

# Non-invasive Characterization of Electron Mach Number in a Hollow Cathode with Incoherent Thomson Scattering

Parker J. Roberts\*, Zachariah Brown†, and Benjamin A. Jorns‡  
 University of Michigan, Ann Arbor, Michigan, 48105

Electron flow is measured non-perturbatively via the incoherent scattering of laser light from electrons in a hollow cathode plume. The scattered spectrum is used to infer the moments of the electron velocity distribution along the axial dimension throughout the expanding cathode plume. Statistical fits of the spectra are employed to compute 1D fluid moments including temperature and mean velocity with uncertainty quantification under assumptions of thermodynamic equilibrium. It is found that electron temperatures range from 4 to 12 eV, flow velocities range from 600 to 1300 km/s, and electron Mach number ranges from 0.3 to 0.8. These results are discussed in the context of previous probe-based estimates for Mach number and in the context of the growth of drift-driven ion acoustic turbulence in the cathode plume.

## I. Nomenclature

$e$	= Elementary charge
$k_B$	= Boltzmann constant
$c$	= Speed of light
$h$	= Planck constant
$n_e$	= Electron density
$T_e$	= Electron temperature
$u_0$	= Electron mean velocity
$\vec{v}$	= Individual electron velocity
$\lambda_D$	= Debye length
$\vec{k}_i$	= Wavevector of incident light
$\vec{k}_s$	= Wavevector of scattered light
$\Delta\vec{k}$	= Shift in wavevector
$\omega_i$	= Angular frequency of incident laser light
$\omega_s$	= Angular frequency of detected laser light
$\Delta\omega$	= Shift in angular frequency
$\theta$	= Angle between incident and scattered wavevector
$\lambda_0$	= Laser wavelength
$f_e(\vec{v})$	= Electron velocity distribution function
$f_e _{\vec{v}\cdot\Delta\vec{k}}$	= Electron velocity distribution projected along scattering vector
$I_s(\omega_s)$	= Intensity spectrum of scattered light
$v_\perp$	= velocity perpendicular to the wavevector shift

## II. Introduction

HOLLOW cathodes, which serve as thermionic electron sources for Hall- and gridded-ion-type electrostatic thrusters, exhibit current-driven instabilities which have a major impact on their operation. Current-carrying cathode plasma plumes commonly display non-classical electron resistivity [1, 2], which increases operating voltages and can decrease overall efficiency of propulsion systems [3]. Additionally, wear tests of hollow cathodes have revealed erosion of the front keeper face [4, 5], which is associated with sputtering erosion from energetic ions impacting the surface [6, 7].

\*Ph.D. Candidate, Aerospace Engineering, AIAA Student Member

†Ph.D. Candidate, Aerospace Engineering, AIAA Student Member

‡Associate Professor, Aerospace Engineering, AIAA Associate Fellow

Both the electron resistivity and the presence of energetic backstreaming ions have been associated with plasma waves which propagate in the cathode plume [8–11]. Since space missions depend on the ability to accurately predict the operation and lifetime of these cathodes, it is essential to account for the impact of these wave effects on the behavior of hollow cathodes by characterizing the mechanisms by which plasma turbulence in the plume grows and saturates.

Ion acoustic turbulence has been widely simulated [10, 12, 13] and experimentally observed [14–16] in hollow cathode plumes. This wave structure propagates via local fluctuations in the electric field and density of the plume plasma, and these variations can exert microscopic forces on electrons and ions which sum to drag-force-like effects which affect macroscopic plasma behavior and even overwhelm the effect of classical collisions [1, 17, 18]. The details of these nonlinear wave-particle interactions depend sensitively on the amplitude of the plasma waves [19], and therefore the energetic mechanisms by which the waves grow and saturate are crucially important. Ion acoustic turbulence is thought to grow in hollow cathodes via streaming instabilities from the directed kinetic energy contained within the electron drift [20, 21]. Since the energy source for the growth of these waves is the streaming velocity of the current-carrying electrons [21], the electron Mach number  $M_e$  is a critical parameter for the determination of the wave growth characteristics, and even the type of waves, if any, that may be present in the plume [9].

Engineering fluid codes must make assumptions about the nature of instability type and growth/saturation throughout the plasma in order to accurately capture these wave-particle interactions, and thus must often be informed by experimental measurements. Efforts to model these phenomena self-consistently, with the wave saturation and growth characteristics derived from the local fluid properties, have been carried out with fluid codes to mixed success using a quasilinear approximation [11, 22–24]. In turn, kinetic models [9, 12] have demonstrated these phenomena from first principles in limited geometries, but the computational cost of these approaches are infeasible for the complex geometries of engineering devices. There is thus a pressing need for experimental methods to accurately and non-intrusively characterize the electron flow properties, so that the nature of streaming instability growth and final saturated amplitude can be predicted self-consistently within fluid codes for rapid iteration and performance prediction.

Previous attempts to measure the electron Mach number in hollow cathodes have been carried out with Langmuir probes in both a steady state [8, 25] and time-resolved [2] sense. These experiments estimated the electron Mach number from the current density and voltage characteristic collected by these probes, and suggested that the growth conditions for ion acoustic turbulence are likely met in the cathode plume. However, the accuracy of these probe measurements are limited by several factors: For one, Langmuir probes collect current through a 3D plasma sheath, so the determination of electron streaming velocities from current collection are quasi-1D at best. Furthermore, inserting physical electrodes into low-temperature plasma devices has been shown to perturb the discharge, and may alter the properties that one is attempting to measure [26, 27].

For this reason, it is necessary to experimentally measure the axial electron Mach number in a hollow cathode plume without perturbing the discharge for the characterization of streaming instability growth conditions. To accomplish this, we implement an incoherent Thomson scattering diagnostic on a standalone hollow cathode without magnetic field. We use a specialized injection geometry to estimate the electron flow and temperature along the axial direction in the cathode plume. Section III describes our experimental approach, including statistical photon-counting techniques as well as fitting methods to obtain statistical moments from measured spectra of scattered laser light from electrons in the plasma. Section IV presents the observed spatial trends in electron density, flow velocity, and temperature. These factors are combined to display approximate Mach number evolution throughout the cathode plume. We also discuss these results in the context of theories of wave saturation and growth, with a mind toward mechanisms which can accelerate ions through quasilinear wave forces and potentially result in increased erosion of cathode keeper surfaces.

### III. Overview of Thomson Scattering

The primary function of the incoherent Thomson scattering (ITS) experiment we employed in this work is to provide a non-invasive measurement of the electron velocity distribution function,  $f_e(\vec{v})$ . From this quantity, we in turn can infer mean fluid properties of interest, such as the average electron velocity (first moment of the distribution), temperature (second moment), and in some cases, the absolute density (zeroth moment). In this section, we summarize the key principles of operation for the diagnostic. Following this, we discuss the details of our experimental implementation as well as our methodology for data analysis.

Figure. 1 shows a top-level illustration of the ITS setup with respect to a hollow cathode. In this case, a beam of coherent laser light with incident wavevector  $\vec{k}_i$  and frequency  $\omega_i$  is injected across the plasma of interest. This light is in turn scattered from the free electrons in the plasma, with a shifted wavevector,  $\vec{k}_s$ , and frequency,  $\omega_s$ . The intensity of this scattered light radiating from a small volume in the plasma is measured with a collection optic focused to that

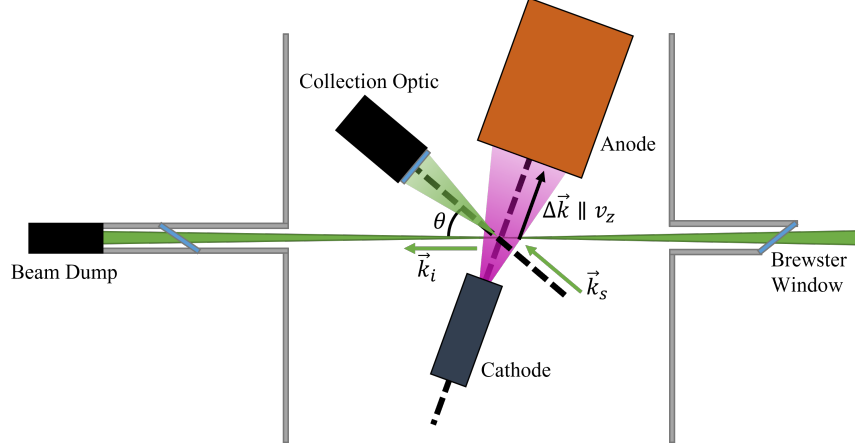


**Fig. 1 a) Schematic of Thomson scattering geometry for the measurement of axial electron velocities in the hollow cathode plume. The obtuse angle between  $\vec{k}_i$  and  $\Delta\vec{k}$  is  $(\pi + \theta)/2$ .**

location, with the optic's normal vector oriented anti-parallel to  $\vec{k}_s$ . The resolution of the measurement location is dictated approximately by the size of the interrogation volume, which is the intersection of the incident laser beam shape with the light path to the collection optic.

The Thomson scattering process is termed "incoherent" for the case where the plasma Debye length  $\lambda_D$  exceeds the laser wavelength  $\lambda_i = 2\pi/k_i$ , and under this assumption the observed spectrum is the sum of the scattered power from individual electron scattering events inside the interrogation volume. Our diagnostic operates in the nonrelativistic regime, where both the incident photon energy  $E_i = hc/\lambda_i$  (where  $h$  is Planck's constant and  $c$  is the speed of light) and the mean electron energy  $k_B T_e$  (where  $k_B$  is Boltzmann's constant) are dwarfed by the electron rest energy  $m_e c^2$ , where  $m_e$  is the electron mass. Within this limit, Thomson scattering from a single electron can be modeled as a classical emission of dipole radiation stimulated by an incident electromagnetic plane wave [28]. We orient the polarization of the incident beam perpendicular to the scattering plane (out of the page in Fig. 1) to maximize the intensity of this dipole radiation [28]. For this scattering process, there is a corresponding shift in angular frequency  $\Delta\omega = \omega_s - \omega_i$  and wavevector  $\Delta\vec{k} = \vec{k}_s - \vec{k}_i$  from the incident to scattered photon. These shifts are related to the projection of the electron velocity along the wavevector shift direction  $\Delta\vec{k}$ :

$$\Delta\omega = \Delta\vec{k} \cdot \vec{v}. \quad (1)$$

In the incoherent scattering limit, the intensity of scattered light collected by the optic is the sum of the power scattered in that direction by all of the electrons within the interrogation volume. Thus, the collected light intensity spectrum is proportional to the distribution of electron velocities along the direction of  $\Delta\vec{k}$  in the interrogation volume:

$$I_s(\omega_s) d\omega_s \propto f_e|_{\vec{v} \cdot \Delta\vec{k}} \left( \Delta\omega / |\Delta\vec{k}| \right) d(\Delta\omega / |\Delta\vec{k}|). \quad (2)$$

Here we have defined the component of the velocity distribution function parallel to  $\Delta\vec{k}$  as

$$f_e|_{\vec{v} \cdot \Delta\vec{k}}(v) = \int f_e(\vec{v}) dv_{\perp} dv_{(\perp \times \Delta\vec{k})}, \quad (3)$$

where  $\hat{\perp}$  and  $\perp \times \hat{\Delta\vec{k}}$  denote the directions perpendicular to  $\Delta\vec{k}$ .

From Eq. 2, we see that by monitoring the intensity spectrum of the scattered signal from the plasma, we can infer a projection of the electron velocity distribution function. We next re-write this result in terms of the scattered wavelength at the collection optic—a parameter we can directly measure spectroscopically. To this end, we note that for nonrelativistic velocities, the change in the magnitude of the shifted wavevector is negligible, i.e.  $|\vec{k}_i| \approx |\vec{k}_s|$ . Assuming an angle  $\theta$  between  $\vec{k}_i$  and  $\vec{k}_s$ , we can then use the law of cosines to write the magnitude of the wavevector shift as  $|\Delta\vec{k}| \approx 2|\vec{k}_i| \sin(\theta/2)$ . Combining this with Eq. 1, we find

$$f_e|_{\vec{v} \cdot \Delta\vec{k}}(v) \propto I_s \left( \frac{\lambda_i}{2v/c \sin(\theta/2) + 1} \right), \quad (4)$$

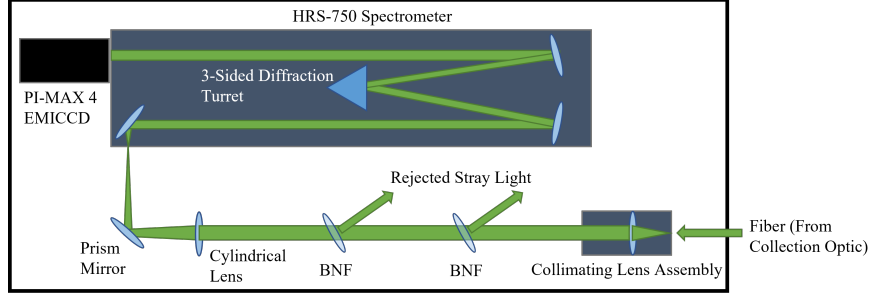


**Fig. 2** Diagram of the optical bench for the analysis of scattered light from the incoherent Thomson scattering process.

where  $\lambda_i$  is the wavelength of the incident laser light.

We see from Eq. 4 that the spectral width of the light intensity spectrum is not only influenced by the spread in velocities, but also the scattering angle  $\theta$ . In reality, light scatters in all directions except for along the polarization axis of the incident light, so  $\theta$  can be chosen judiciously for the detection bandwidth of a given detector. For angles below  $90^\circ$ , increasing  $\theta$  corresponds to increasing the apparent spectral width. While increasing the spectral dispersion can be advantageous for resolving local features of the velocity distribution, this broadening also reduces the intensity in a given wavelength range, which may be of detriment to signal-to-noise ratio (SNR).

In order to measure the scattered spectrum and infer the properties of the electron velocity distribution, we couple the collected light to a spectrometer system which detects the intensity of light as a function of scattered wavelength. While in this work we measure the unnormalized velocity distribution to infer mean velocity and temperature of the electrons, in principle, the factors of proportionality relating the absolute intensity of light to the height of the electron distribution can be calibrated through other well-understood light scattering processes to allow electron density measurements [28, 29].

## IV. Experimental Setup

### A. Test Article

The test article for this experiment was a 60-A-class hollow cathode designed for use with the 9-kW H9v2 Hall thruster [30]. We operated this cathode with no magnetic field in the University of Michigan's Cathode Test Facility (CTF), a 1-meter-long cylindrical vacuum chamber with a diameter of 0.6 m. A cylindrical anode with an inner diameter of 75 mm collected electrons to sustain the discharge. We supplied a stream of water to cool the anode, which was located 300 mm downstream of the cathode. For all scattering measurements, the cathode was operated on xenon at 1.34 mg/s flow (15 sccm at  $25^\circ\text{C}$ ), while a discharge power supply maintained a constant current of 15 A. Previous Langmuir probe measurements of this cathode operating in a Hall thruster at 15 A showed plasma densities in excess of  $6 \cdot 10^{17} \text{ m}^{-3}$  at a distance of 25 mm from the cathode face [31]. Throughout the test, the discharge voltage remained relatively steady at 23-25 V. The keeper voltage was allowed to float to 5 V, but the current flowing from the keeper was turned off during operation. During operation, the chamber pressure rose from a base of 2.6 to 240  $\mu\text{Torr}$ .

### B. Optical bench

We implemented a compact Thomson scattering diagnostic based on the design principles established in Ref. [29]. For the scattering source, we employed a Quanta-Ray Pro Nd:YAG laser. This is a Q-switched, solid-state laser which operates at the second YAG harmonic of 532 nm. The laser emits  $\sim 700\text{-mJ}$  pulses at a fixed repetition rate of 10 Hz, with a pulse duration  $< 10$  ns. Two 50-mm-diameter mirrors in a periscope configuration direct light from the laser into the chamber. A convex lens between the periscope mirrors focuses the  $\lesssim 1\text{-cm}$ -diameter beam to a spot  $\sim 1$  mm in size in the cathode plume. The light enters the chamber by passing through a fused-silica Brewster window to minimize internal reflections at the air-vacuum interface, which would otherwise lead to increased stray light reaching the detector. The window is held at the Brewster angle by a custom flange based on the design in Ref. [32], and we used an aluminum mounting plate to sink absorbed heat from the beam away from the optic. The light then exits the chamber after traversing the cathode plasma through a second Brewster window, after which it is incident on a water-cooled laser

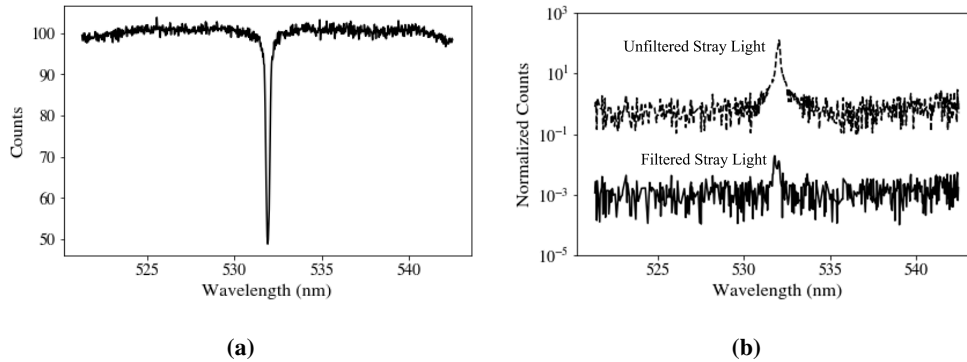


**Fig. 3 Effect of dual Bragg notch filters. a) Bragg filtering of a broadband light source. b) Comparison between unfiltered and filtered stray laser light spectra. The different background noise floors are due to different camera gain settings.**

beam dump to absorb the majority of the residual beam energy not scattered by the plasma.

Within the chamber, a 25-mm-diameter collection lens focuses scattered photons into a multimode optical fiber with diameter 200  $\mu\text{m}$ . The interrogation volume, defined as the intersection of the laser beam at its waist with the cone formed by the collection optic light path, is  $\sim 1 \text{ mm}^3$  in volume. The lens is a perpendicular distance of 100 mm from the interrogation spot, representing a solid angle of 0.05 sr. We mounted the hollow cathode on a linear motion stage aligned with the cathode axis in order to move the collection spot relative to the plume. The maximum scattering angle that could be achieved given the dimensions of the chamber and the motion stage was  $\theta = 22^\circ$ . The collection optic was also mounted on fine motorized stages in order to adjust alignment to maximize scattering signal.

The fiber passes collected light through a potted vacuum feedthrough to a detection optics table, which is covered by a light-blocking sheet to shield the optics from ambient light. Figure 2 shows a diagram of this detection apparatus. The output beam from the fiber is first collimated by an adjustable lens assembly, before passing through two ultra-narrow-bandwidth Bragg notch filters in series. These are volume Bragg grating optics which are designed to reduce the intensity of light at the laser wavelength, which is a combination of stray light from reflections and Rayleigh scattering signal from the gas, by several orders of magnitude [33]. These filters are highly sensitive to angular alignment, so they are mounted on precise rotation stages which allow fine angular control.

Figure 3 displays the measured filtering spectrum of these optics, as measured by the reduction in intensity of a broadband light source within each wavelength bin measured by the detector. The  $\sim 1\text{-nm}$  spectral width of the filter is measured by filtering a broadband light source (Fig. 3a), while the peak optical density (OD) of  $\sim 4$  is demonstrated by comparing the intensity of the stray laser light before and after the filters are aligned (Fig. 3b). It is possible that with improved collimation, these filters could be aligned up to OD 7-8 [33]. After passing through the dual filtering stage, a cylindrical lens focuses the collected light to the slit plane of an HRS-750 triple-grating spectrometer, which diffracts the light onto the detection plane of a PI-MAX 4 camera. This is an advanced low-light camera which makes use of electron-multiplying intensified charge-coupled device (EMICCD) technology. We used a spectrometer grating of 1200 g/mm centered at 532 nm, which projected the wavelength spectrum onto the 760 columns of CCD pixels. For the  $\theta = 22^\circ$  scattering angle used in this experiment, this corresponds to a velocity resolution of  $\sim 20 \text{ km/s}$ . We calibrated the wavelength measurement of the spectrometer and camera with known emission lines from an arc lamp light source, provided by the spectrometer manufacturer, to align the rotation of the camera and spectrometer optics automatically.

A timing pulse from the laser Q-switch trigger was used to activate the camera photocathode, beginning CCD exposure after a hand-tuned delay of several hundred nanoseconds. By experimenting with different gate widths on the Rayleigh and Raman scattering signal from a neutral gas, we found that an exposure gate width of 20 ns after this trigger delay enabled the capture of essentially all light scattered during the pulse. We grouped exposures into acquisitions of 300 frames, where each frame consists of the software average of 10 sequential exposures. In order to operate the camera at the 10 Hz laser repetition rate, we also binned the vertical axis of 760x760 CCD pixels into 10 rows of 76 pixels, which enabled faster pixel readout. The spectrometer maps light of different wavelengths along the horizontal axis of the CCD chip, so each column of pixels is calibrated to correspond with a particular range of wavelengths, according to the spectrometer grating used. For this experiment, the detected light intensity was sufficiently dim that few photons were observed per 10-exposure frame, meaning that individual photoelectron events were identifiable.

When photons are incident on CCD pixels, the light is represented as a stored charge with a success rate according to the quantum efficiency of the detector [34]. Intensified (I)CCDs utilize a photoluminescent phosphor stage for analog amplification of light intensity before impacting the detector. In electron-multiplying (EM) ICCDs, this analog multiplication process is combined with a digital multiplication process to resolve signals in even lower light conditions. For electron multiplication, stored charge from an exposure is amplified by passing the charge in each pixel through a serial register of many charge storage modules with high voltages, leading to a small probability of producing further electrons through impact ionization at each transfer event. In bulk, this charge transfer process results in amplification of the initial, potentially faint photoelectron signal by a gain factor of several thousand. We set EMICCD gain values to 5000 for this experiment, which yielded clearly observable single-photon events without causing excessive "blooming" of charge into neighboring pixels.

## V. Analysis Methodology

Despite the hardware we employed to reduce stray light and improve signal gain, the signal to noise for Thomson scattering in the low density cathode environment poses a major challenge for extracting the electron velocity distribution. To this end, we overview in the following section our methodology for isolating the Thomson signal and inferring the electron properties from it.

### A. Thresholding algorithm for photon counting

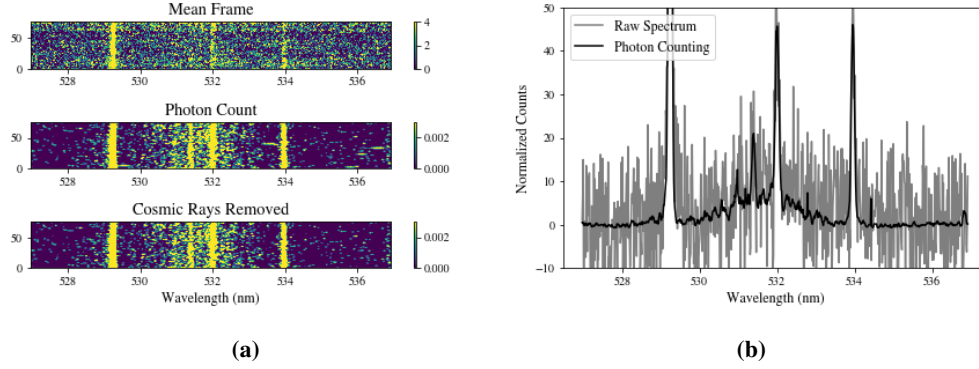
Due to the low electron scattering cross section [28], only a small number of photons from the Thomson scattering process were detected during a single laser pulse. Therefore, to build up sufficient signal-to-noise to identify the spectral shape, we averaged the acquisitions over many laser shots. For this work, we average 9,000 shots for each position in the cathode plume. At the laser's repetition rate of 10 Hz, this equates to 15 minutes of acquisition with the laser on, with an additional 15 minutes to characterize the background spectrum with the laser off. The values of light intensity measured by the camera pixels are subject to background electrical noise, which is characterized via background acquisitions with the laser and plasma off. The signal was also corrupted by random, spurious photoelectrons that arose from imperfections within the camera's serial register during the charge amplification process, as well as from cosmic ray particles impacting the camera chip and causing large spikes. Finally, the "shot noise" associated with the fundamental quantum uncertainty in the photon-production process contributes to uncertainty in the Thomson signal; this noise in arrival frequency can be described as Poisson in distribution [35, 36].

To overcome these noise sources, we implemented a thresholding algorithm before averaging the camera frames to identify and count individual photoelectron detection events, following the work of Ref. 36. For an EMICCD gain of 5000, we set a photon count threshold of 50 counts, and set the value of each pixel above this threshold to 1 count, with the rest set to zero counts. The raw value of counts recorded by each pixel is proportional to the light intensity which falls on that pixel during the camera exposure. After photon thresholding is applied, the frames are averaged to yield a combined frame representing the We also implemented an analogous filter to remove cosmic rays, where pixel values above a threshold of 2000 were set to zero. Cosmic rays manifested as sections of neighboring pixels with large count values of several thousand, while individual photons from the scattering process generally occurred in the 60-200-count range. Fig. 4 demonstrates the effect of this discrete filtering on the raw frame and resulting spectrum for a Thomson acquisition. While there are subtle emission lines present in the plasma background which are buried by CCD noise in the raw trace, these features become prominent after this photon counting is applied. Figure 4a also shows the removal of large splotches on the frame corresponding to cosmic ray detection events.

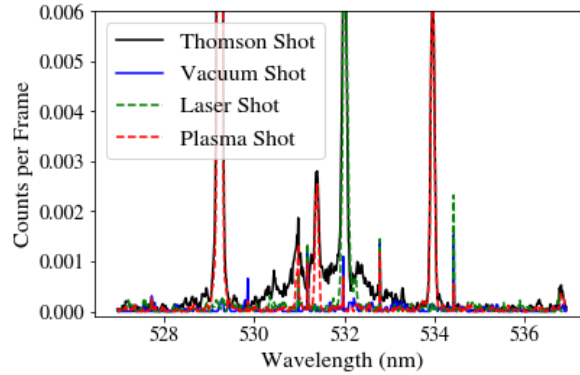
### B. Removal of background spectrum and scattered light

Figure 5 displays a Thomson acquisition overlaid with various background acquisition conditions after the thresholding algorithm was applied: the laser operating with the cathode off, the cathode operating with the laser off, and a dark background shot to characterize the pixel noise. We observed thermal drifts in the background mean pixel values, which we minimized by taking background traces in-between each 5-minute set of 3,000 laser shots. This also served the purpose of allowing the injection Brewster window to cool between series of laser shots to avoid thermal damage. After photon counting, the electrical noise spectrum (blue) is reduced to the point of being nearly negligible in most cases. Figure 5 shows strong spectral lines not only from stray light and Rayleigh scattering signal at the laser wavelength (green), but also from emission lines of the plasma within the collection volume (red).

While some large emission lines occur at 529.3 and 534 nm outside of the Thomson spectrum shown and do not



**Fig. 4** Effect of photon-counting and cosmic-ray-suppression algorithm on raw 3000-shot spectrum acquisitions. a) Denoising of 2D camera frame with pixel count thresholding, where the colormap represents light intensity for each pixel. b) Resulting Thomson spectrum before and after denoising.



**Fig. 5** Overlay of Thomson scattering acquisition at 8 mm from the cathode, with overlaid background spectra with the laser only, plasma only, and a dark background spectrum.

interfere with the measured spectrum, there are weaker emission lines from the background plasma which overlap with the spectrum between 531 and 532 nm. To minimize the effect of these emission lines on the Thomson result, we subtract the plasma background spectrum from the Thomson spectrum before fitting and analysis. However, we acknowledge that variability in the intensity of these lines between shots may introduce additional uncertainty into fit parameters. For acquisitions < 6 mm from the cathode face, the reflected stray light signal was so intense that the wings of the laser line overlapped significantly with the Thomson spectrum - to overcome this, we subtracted both the plasma background spectrum and the laser spectrum from these acquisitions to determine the Thomson signal. For locations further from the keeper where the stray light contribution was lower, we only subtracted the plasma background spectra so as to not introduce additional noise from the subtraction process. At a distance greater than 14 mm from the cathode exit, the signal was sufficiently low that a good fit was not obtainable even after denoising.

### C. Model for fitting measured electron velocity distribution function

After we apply the signal conditioning and subtraction developed in the preceding sections, we have a measured spectrum given approximately by Eq. 4. We show an example spectrum in Fig. 6a. In principle, this distribution could have an arbitrary shape dictated by local kinetic effects in the plasma. Indeed, for higher signal-to-noise ratio acquisitions, the capability to identify specific nonequilibrium features in the shape of the distribution could be advantageous for the identification of wave-particle interactions. However, given the relatively low signal in the current experimental setup, these features may not be possible to resolve above the noise. As an alternative, we make the assumption that the distribution is thermalized such that we can employ a 1D Maxwellian (Gaussian) model to represent the measured

distribution:

$$I_{model}(\lambda_s) = A \exp \left[ - \left( \frac{v(\lambda_s) - u_0}{v_{T_e}} \right)^2 \right], \quad (5)$$

where  $A$  represents the overall height (intensity) of the distribution,  $u_0$  represents the bulk electron drift velocity along the wavevector shift axis, and  $v_{T_e} = \sqrt{2k_B T_e / m_e}$  is the thermal electron velocity, with  $T_e$  being the electron temperature. We observe a spectrum over scattered wavelength  $\lambda_s$  with the camera, but the wavelength axis may be converted to electron velocity via the Doppler relation  $v(\lambda_s)$  (Eq. 4). We therefore apply this conversion and fit the measured spectrum to the model in Eq. 5 using a nonlinear least squares algorithm.

The 3 parameters of this fit are  $A$ ,  $u_0$ , and  $T_e$ , which respectively give the approximate electron density, axial flow speed, and temperature at the measured location. To obtain the relative density, we can compare the form of the wavelength spectrum in Eq. 5 to the form of a normalized 1-dimensional Maxwellian distribution [37] via the relation

$$A \propto n_e \sqrt{\frac{m}{2\pi k_B T_e}}. \quad (6)$$

The proportionality factor in Eq. 6 depends on geometric parameters of the scattering setup such as the optical transmission of the detection system and the solid angle subtended by the collection optic. While in future studies we plan to obtain absolute calibration of these proportionality factors via well-characterized scattering processes from neutral gases, in this work we focus on the higher moments of the electron velocity distribution and only report normalized density values of the form  $\bar{n}_e \propto A \sqrt{T_e}$ .

#### D. Deconvolution of instrument broadening

The spectrometer slightly blurs input light with a finite-width instrument function over multiple nearby pixels on the detector. This blurring leads to an artificial broadening of the observed intensity spectrum, which can be modeled as the convolution of the true spectrum with the instrument function of the spectrometer. In order to obtain accurate electron temperature information, it is crucial to remove the effect of this broadening on the collected spectra. To reconstruct the deconvolved spectrum, we follow the approach of Ref. 29 in approximating the true spectrum of the laser as a delta function in wavelength. This allows us to use the spectrum obtained from an unfiltered stray laser light shot in vacuum to infer the shape of the instrument function. The unfiltered spectrum shown in Fig. 3 displays an example of this spectral shape. We smooth the instrument function  $H(\lambda_s)$  and normalize it by the area under the curve as calculated with a trapezoidal integration, so that

$$\int H(\lambda_s) d\lambda_s \approx 1. \quad (7)$$

In practice, it is difficult to reconstruct the actual spectrum through numerical deconvolution by the measured instrument function. This is because the deconvolution is highly sensitive to noise in the signal. However, we can account for this blurring effect in the fitting parameters by incorporating the forward convolution operation as part of the fitting function. We therefore represent the model for the measured spectrum as the forward convolution of the Maxwellian fitting function developed in Eq. 5 with the instrument function, to reach the broadened fit spectrum

$$I_{fit}(\lambda_s) = I_{model} * H(\lambda_s) = \int I_{model}(L) \cdot H(L - \lambda_s) dL. \quad (8)$$

We implement this convolution numerically as part of the fitting function in the nonlinear least squares fits of the processed spectra. This serves as a correction for the distortion of the "true" spectrum according to the spectral broadening properties of the spectrometer and more accurately fit the observed spectrum.

## VI. Results & Discussion

In this section, we discuss the electron properties inferred from the Thomson scattering experiment at various positions on the cathode plume axis. We then address these results in the context of previous probe measurements of the electron properties in hollow cathode experiments, as well as the relation of these data to models for wave growth and saturation.

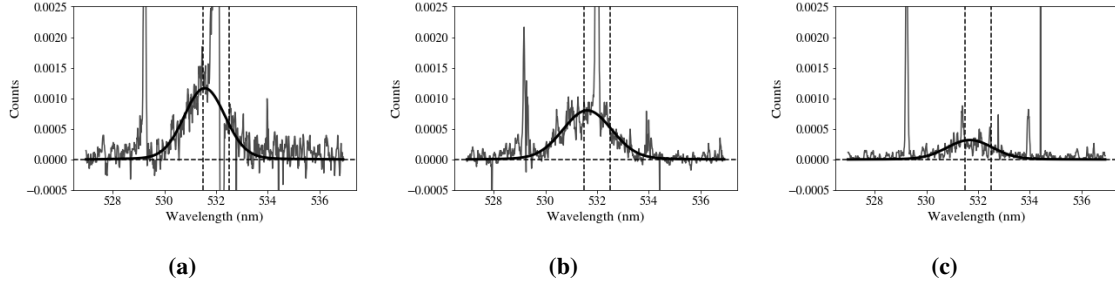


**Fig. 6** Examples of Thomson spectra after photon-counting and background subtraction are applied. Signal within the filter stopband, shown as dashed vertical lines, is rejected from the fit. A Gaussian fit is used for points outside of this range, shown as a thick line. a) 5.2 mm from the cathode exit. b) 7.8 mm from the cathode exit. c) 11.7 mm from the cathode exit.

### A. Thomson Spectrum Analysis

Figure 6 displays examples of processed Thomson spectra at different axial positions. The vertical axes correspond to average counts per frame within each wavelength bin. We acquired scattering spectra at positions ranging from 5 mm to 13 mm from the cathode keeper face. Acquisitions closer than 5 mm to the cathode exit were obscured by a prohibitively large quantity of stray light reflecting from the cathode surfaces and into the collection optic, precluding measurements here without damaging the detector. Likewise, at distances exceeding 13 mm, the signal intensity fell off to the point that it was indistinguishable from the noise, likely due to the lowering of the electron density as the plume expands. However, in the intermediate range between 5 and 13 mm from the keeper face, the relative contributions of stray light and camera noise were sufficiently low to observe a number of Thomson photons, enabling the construction of spectra for fitting. Figure 6 demonstrates that the Maxwellian fitting scheme described in Section V.C was able to match the shape of the spectra reasonably well.

In Figs. 7 and 8, we display the trends in electron properties inferred from these fits as a function of axial position. Error bars are computed from the standard error in the nonlinear least squares fitting process. Figure 7a displays electron temperatures ranging from 4 to 11 eV. No significant overall trend is observed in the electron temperatures. The temperature appears to dip to an outlier value of 4 eV at the axial position 9.1 mm from the cathode face. Previous measurements of the electron temperature with emissive and Langmuir probes [2, 8], as well as non-axial Thomson scattering [38], generally show lower  $T_e$  values below 5 eV, with the temperature relatively constant or increasing as a function of axial position.

With this in mind, at least two interpretations are possible for this temperature data. Firstly, it may be that the poor signal-to-noise in the spectra resulted in higher variability in the fit parameters than is represented by the mean standard error bars from the nonlinear least squares optimization. A second possibility is that the points beyond 8 mm from the plume are more trustworthy than the upstream points due to the lower quantity of laser stray light observed in the spectrum. If the deconvolution and subtraction algorithms failed to account for some additional broadening caused by the stray laser light and Rayleigh signal at the laser wavelength, it is possible that the smooth increase in temperature observed from 6 to 13 mm is legitimate, and the width of the upstream velocity distributions are artificially increased by the wings this laser signal or the plasma emission line spectrum. We also recognize that based on previous measurements and simulations, large gradients in the fit parameters likely exist near the cathode exit, upstream of the interrogated domain in this experiment. Future efforts will therefore aim toward the further reduction of stray light and increasing of signal-to-noise ratio in order to achieve higher-confidence temperature measurements in the upstream region of the plume.

The axial electron flow velocities, shown in Fig. 7b, range from 800 to 1300 km/s. A slight increase in this flow speed with axial position is apparent. Emissive probe measurements of the plasma potential in a similar cathode setup display an increase in the plasma potential with axial position, as expected due to the DC discharge maintained by the power supply via the anode current [2]. Our measurements of the flow velocity increasing are consistent with this picture of electrostatic acceleration.

While we did not calibrate the diagnostic intensity to measure absolute electron density in this experiment, the relative intensity of the spectra is proportional to the electron density. Figure 8a shows the variation in the intensity of the spectrum, as measured by the height and width of the velocity distribution according to  $\bar{n}_e \propto A\sqrt{T_e}$  (Eq. 5). We see

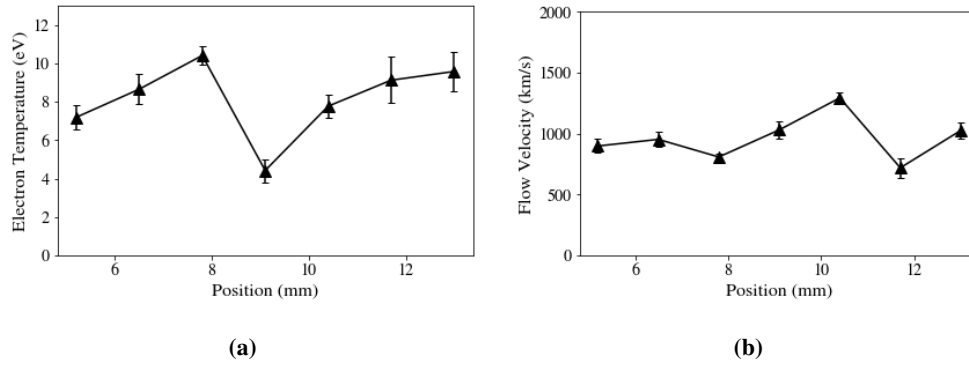


**Fig. 7** Fit parameters obtained from the axial Thomson spectra collected at various positions in the cathode plume. The amplitude of the distribution is proportional to the uncalibrated density of the electron population.

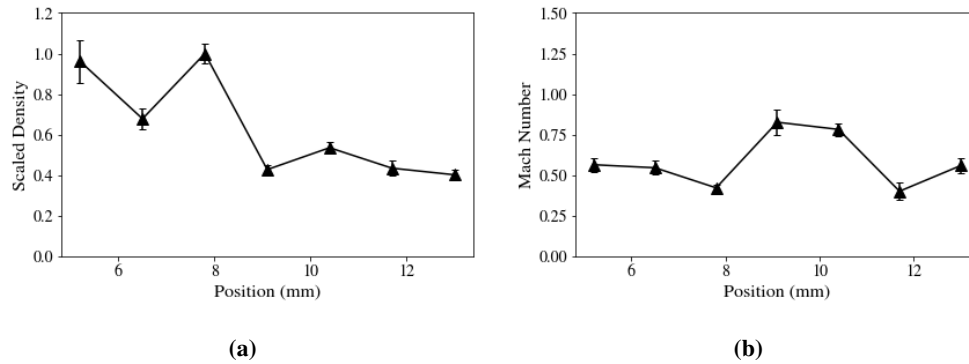


**Fig. 8** a) Relative (uncalibrated) electron density, scaled to the maximum value. b) Estimated axial Mach number.

that the density generally decreases with axial distance from the cathode, as expected due to the expansion of the plume. We observe a local maximum in the density at roughly 9 mm from the cathode. Other measurements of the electron density in hollow cathodes with probes [2] and off-axis Thomson scattering [38] generally observe a monotonically decreasing density profile, which is consistent with the general trend of the Thomson data but not the point-by-point behavior.

We compute the axial Mach number as the ratio of the electron flow speed to the thermal velocity,  $M_e = u_0/v_{Te}$ . The spatial variation of this dimensionless parameter according to the above moment calculations is shown in Fig. 8b. We observe Mach numbers between 0.3 and 0.8 across the interrogated domain. While no strong trend in Mach number is apparent, the point-to-point variability unsurprisingly appears to be strongly influenced by the variation in the electron drift velocity. The exception to this is the measurement at 9.1 mm, in which case the significantly lower temperature elevates the Mach number despite the this location's comparable drift velocity to other nearby points. We note that while the bulk electron population is subsonic in this region according to this diagnostic, there are non-negligible numbers of supersonic electrons present in the tails of these velocity distributions.

The variability in the data and discrepancies compared to Langmuir probe data likely imply that the true uncertainty in these fit parameters exceeds the error bars generated by the fitting process, due to excessive noise in the spectra. Still, to the authors' knowledge this represents the first direct light scattering measurement of the axial electron flow velocity in a hollow cathode, and future improvements will likely yield improved signal-to-noise with increased confidence over an expanded domain. Furthermore, previous non-axial Thomson scattering measurements of isotropic cathode electron temperature reveal large discrepancies with Langmuir probe measurements [38], suggesting that further validation work and analysis of the perturbative effect of probes is necessary for validation between diagnostic forms.

## B. Implications for Instability Growth

Previous efforts to evaluate the growth of ion acoustic turbulence in hollow cathodes demonstrate the sensitivity of the results to the value of the electron Mach number, since the electron streaming velocity serves as the mechanism for wave energy growth. Indeed, analytical formulations of the ion acoustic wave energy density as a function of local plasma fluid properties show that the growth rate of these modes is directly proportional to the electron Mach number [14, 25], and simulations built on these wave models demonstrate strong correlations between anomalous electron transport coefficients and electron Mach number [24]. Kinetic models [9, 12] can replicate the growth of these modes from first principles, demonstrating that the final, observed electron properties depend on the nature of the equilibrium state reached after wave saturation. Fluid models aiming to capture wave-particle interactions to predict cathode performance have relied on Langmuir probe current density measurements to estimate the Mach number; these techniques are suspect due to the 3D nature of probe current collection and the perturbative nature of these electrode-based diagnostics [8, 25]. The diagnostic configuration presented in this work therefore improves upon the recent development of incoherent Thomson scattering capabilities for low-temperature plasmas in order to measure the electron streaming velocities along the axial direction. Though these measurements are subject to noise due to the low light levels, the Thomson scattering experiment presented herein represents a more direct method for inferring the electron temperature and drift speed via a non-perturbative means. This work thus provides a powerful tool for the characterization of mechanisms for the growth and saturation of streaming instabilities in hollow cathodes and other low-temperature plasma sources.

## VII. Conclusions

We implemented a non-perturbative incoherent Thomson scattering diagnostic to measure the axial electron flow properties in a standalone hollow cathode plume. We achieved this by injecting a beam of monochromatic radiation from a high-power pulsed laser, and collecting the light scattered by the plasma within a small spot along this beam. High-efficiency optical notch filters and an advanced EMICCD camera enabled the reduction of stray light in order to observe the Thomson spectrum near the laser wavelength. Low-light signal was separated from noise through a thresholding algorithm to count single-photon events, and the resulting spectrum was related to the electron velocity distribution function via the effect of Doppler broadening on the scattering wavelength. We fit these spectra assuming Maxwellian electron distributions, and accounting for the artificial broadening occurring due to the convolution of spectra with the spectrometer instrument function. The moments of these fits correspond to electron fluid properties, including the mean drift velocity, electron temperature, and relative density.

We observed relative electron density to decrease with expansion away from the cathode. Electron temperatures ranged from 4 to 11 eV, generally increasing with axial distance, although significant variability was shown in the data. Axial flow velocities were observed between 600 and 1300 km/s away from the cathode. This resulted in electron Mach numbers from 0.3-0.8. While the electron population as a whole is subsonic throughout the plume according to these measurements, we observe a number of supersonic electrons present in the distributions due to their width. These measurements of electron Mach number roughly correspond with previous measurements of this value with Langmuir probes. Temperature values are generally higher than typical Langmuir probe measurements by a factor of 2, which is suggestive of a discrepancy between these diagnostics which must be resolved in future validation work through increased signal-to-noise acquisitions and modeling of the perturbative effect of Langmuir probes near the cathode. Despite this temperature discrepancy, the approximate size of the electron Mach number we observe in this experiment does roughly correspond with other measurements of this parameter being below 0.5. This study represents the first application, to our knowledge, of incoherent Thomson scattering to measure axial electron velocities in a hollow cathode. In future work, we plan to modify the experimental parameters to increase signal-to-noise and block stray light with higher efficiency, in order to characterize the electron velocities closer to the cathode exit and with higher confidence. We also hope to apply this diagnostic to measure electron streaming characteristics in related low-density plasma propulsion devices.

## Acknowledgments

This work was supported by a NASA Space Technology Graduate Research Opportunity (Grant 80NSSC20K1229).

## References

- [1] Mikellides, I., Katz, I., Goebel, D., and Jameson, K., "Evidence of Non-Classical Transport in Discharge Hollow Cathodes," *APS Division of Plasma Physics Meeting Abstracts*, Vol. 48, 2006, pp. NO2-013.

- [2] Georgin, M. P., Jorns, B. A., and Gallimore, A. D., “Transient non-classical transport in the hollow cathode plume I: measurements of time-varying electron collision frequency,” *Plasma Sources Science and Technology*, Vol. 29, No. 10, 2020, p. 105010.
- [3] Su, L. L., and Jorns, B., “Performance at high current densities of a magnetically-shielded Hall thruster,” *AIAA Propulsion and Energy 2021 Forum*, 2021, p. 3405.
- [4] Frieman, J. D., Gilland, J. H., Kamhawi, H., Mackey, J., Williams Jr, G. J., Hofer, R. R., and Peterson, P. Y., “Wear trends of the 12.5 KW HERMeS Hall thruster,” *Journal of Applied Physics*, Vol. 130, No. 14, 2021, p. 143303.
- [5] Sengupta, A., Anderson, J. A., Garner, C., Brophy, J. R., de Groh, K. K., Banks, B. A., and Thomas, T. A. K., “Deep space 1 flight spare ion thruster 30,000-hour life test,” *Journal of Propulsion and Power*, Vol. 25, No. 1, 2009, pp. 105–117.
- [6] Mikellides, I. G., and Katz, I., “Wear mechanisms in electron sources for ion propulsion, I: Neutralizer hollow cathode,” *Journal of Propulsion and Power*, Vol. 24, No. 4, 2008, pp. 855–865.
- [7] Mikellides, I. G., Katz, I., Goebel, D. M., Jameson, K. K., and Polk, J. E., “Wear mechanisms in electron sources for ion propulsion, II: Discharge hollow cathode,” *Journal of Propulsion and Power*, Vol. 24, No. 4, 2008, pp. 866–879.
- [8] Jorns, B., Goebel, D. M., and Mikellides, I. G., “Investigation of energetic ions in a 100-a hollow cathode,” *50th AIAA/ASME/SAE/ASEE Joint Propulsion Conference*, 2014, p. 3826.
- [9] Hara, K., and Treece, C., “Ion kinetics and nonlinear saturation of current-driven instabilities relevant to hollow cathode plasmas,” *Plasma Sources Science and Technology*, Vol. 28, No. 5, 2019, p. 055013.
- [10] Hara, K., “High-energy ion generation due to the plasma wave driven by current-carrying instabilities,” *AIAA Propulsion and Energy 2019 Forum*, 2019, p. 4249.
- [11] Georgin, M. P., and Jorns, B. A., “Transient non-classical transport in the hollow cathode plume II: evaluation of models for the anomalous collision frequency,” *Plasma Sources Science and Technology*, Vol. 29, No. 10, 2020, p. 105011.
- [12] Hara, K., and Kubota, K., “Direct kinetic simulation of ion acoustic turbulence in cathode plume,” *35th International Electric Propulsion Conference, Atlanta, Georgia, IEPC-2017*, Vol. 496, 2017.
- [13] Kubota, K., Oshio, Y., Watanabe, H., Cho, S., and Funaki, I., “Numerical simulation of hollow cathode with hybrid-PIC coupled with growth model of ion acoustic turbulence,” *2018 Joint Propulsion Conference*, 2018, p. 4513.
- [14] Jorns, B. A., Mikellides, I. G., and Goebel, D. M., “Ion acoustic turbulence in a 100-A LaB 6 hollow cathode,” *Physical Review E*, Vol. 90, No. 6, 2014, p. 063106.
- [15] Yanes, N., Jorns, B., Friss, A., Polk, J. E., Guerrero, P., and Austin, J. M., “Ion acoustic turbulence and ion energy measurements in the plume of the HERMeS thruster hollow cathode,” *52nd AIAA/SAE/ASEE Joint Propulsion Conference*, 2016, p. 5028.
- [16] Georgin, M. P., Jorns, B. A., and Gallimore, A. D., “Correlation of ion acoustic turbulence with self-organization in a low-temperature plasma,” *Physics of Plasmas*, Vol. 26, No. 8, 2019, p. 082308.
- [17] Sagdeev, R. Z., and Galeev, A. A., “Nonlinear plasma theory,” *Nonlinear Plasma Theory*, 1969.
- [18] Bychenkov, V. Y., Silin, V. P., and Uryupin, S., “Ion-acoustic turbulence and anomalous transport,” *Physics Reports*, Vol. 164, No. 3, 1988, pp. 119–215.
- [19] Roberts, P. J., Jorns, B. A., and Chaplin, V. H., “Experimental Characterization of Wave-Induced Azimuthal Ion Velocities in a Hollow Cathode Plume,” *AIAA SCITECH 2022 Forum*, 2022, p. 1561.
- [20] Stringer, T., “Electrostatic instabilities in current-carrying and counterstreaming plasmas,” *Journal of Nuclear Energy. Part C, Plasma Physics, Accelerators, Thermonuclear Research*, Vol. 6, No. 3, 1964, p. 267.
- [21] Buneman, O., “Dissipation of Currents in Ionized Media,” *Phys. Rev.*, Vol. 115, 1959, pp. 503–517. <https://doi.org/10.1103/PhysRev.115.503>, URL <https://link.aps.org/doi/10.1103/PhysRev.115.503>.
- [22] Jorns, B., Lopez Ortega, A., and Mikellides, I. G., “First-principles modelling of the IAT-driven anomalous resistivity in hollow cathode discharges I: Theory,” *52nd AIAA/SAE/ASEE Joint Propulsion Conference*, 2016, p. 4626.
- [23] Lopez Ortega, A., Mikellides, I. G., and Jorns, B., “First-principles modeling of the IAT-driven anomalous resistivity in hollow cathode discharges II: Numerical simulations and comparison with measurements,” *52nd AIAA/SAE/ASEE Joint Propulsion Conference*, 2016, p. 4627.

- [24] Lopez Ortega, A., Jorns, B. A., and Mikellides, I. G., "Hollow cathode simulations with a first-principles model of ion-acoustic anomalous resistivity," *Journal of Propulsion and Power*, Vol. 34, No. 4, 2018, pp. 1026–1038.
- [25] Jorns, B. A., Dodson, C., Goebel, D. M., and Wirz, R., "Propagation of ion acoustic wave energy in the plume of a high-current LaB 6 hollow cathode," *Physical Review E*, Vol. 96, No. 2, 2017, p. 023208. <https://doi.org/10.1103/PhysRevE.96.023208>, URL <https://link.aps.org/doi/10.1103/PhysRevE.96.023208>.
- [26] Jorns, B., Goebel, D. M., and Hofer, R. R., "Plasma perturbations in high-speed probing of Hall thruster discharge chambers: Quantification and mitigation," *51st AIAA/SAE/ASEE Joint Propulsion Conference*, 2015, p. 4006.
- [27] Lobbia, R. B., and Beal, B. E., "Recommended practice for use of Langmuir probes in electric propulsion testing," *Journal of Propulsion and Power*, Vol. 33, No. 3, 2017, pp. 566–581.
- [28] Sheffield, J., Froula, D., Glenzer, S. H., and Luhmann Jr, N. C., *Plasma scattering of electromagnetic radiation: theory and measurement techniques*, Academic press, 2010.
- [29] Vincent, B., Tsikata, S., Mazouffre, S., Minea, T., and Fils, J., "A compact new incoherent Thomson scattering diagnostic for low-temperature plasma studies," *Plasma Sources Science and Technology*, Vol. 27, No. 5, 2018, p. 055002.
- [30] Hofer, R. R., Cusson, S. E., Lobbia, R. B., and Gallimore, A. D., "The H9 magnetically shielded Hall thruster," *35th International Electric Propulsion Conference*, Electric Rocket Propulsion Soc., 2017, pp. 2017–232.
- [31] Jorns, B. A., Cusson, S. E., Brown, Z., and Dale, E., "Non-classical electron transport in the cathode plume of a Hall effect thruster," *Physics of Plasmas*, Vol. 27, No. 2, 2020, p. 022311.
- [32] Asvany, O., Krüger, H., and Schlemmer, S., "Simple O-ring sealed Brewster-angle window for ultrahigh vacuum applications," *Journal of Vacuum Science & Technology B, Nanotechnology and Microelectronics: Materials, Processing, Measurement, and Phenomena*, Vol. 38, No. 4, 2020, p. 045001.
- [33] Glebov, A. L., Mokhun, O., Rapaport, A., Vergnole, S., Smirnov, V., and Glebov, L. B., "Volume Bragg gratings as ultra-narrow and multiband optical filters," *Micro-Optics 2012*, Vol. 8428, SPIE, 2012, pp. 42–52.
- [34] Denvir, D. J., and Conroy, E., "Electron-multiplying CCD: the new ICCD," *Low-Light-Level and Real-Time Imaging Systems, Components, and Applications*, Vol. 4796, SPIE, 2003, pp. 164–174.
- [35] Dussault, D., and Hoess, P., "Noise performance comparison of ICCD with CCD and EMCCD cameras," *Infrared Systems and Photoelectronic Technology*, Vol. 5563, SPIE, 2004, pp. 195–204.
- [36] Basden, A., Haniff, C., and Mackay, C., "Photon counting strategies with low-light-level CCDs," *Monthly notices of the royal astronomical society*, Vol. 345, No. 3, 2003, pp. 985–991.
- [37] Bellan, P. M., *Fundamentals of plasma physics*, Cambridge university press, 2008.
- [38] Vincent, B., Tsikata, S., Potrivitu, G.-C., Garrigues, L., Sary, G., and Mazouffre, S., "Electron properties of an emissive cathode: analysis with incoherent Thomson scattering, fluid simulations and Langmuir probe measurements," *Journal of Physics D: Applied Physics*, Vol. 53, No. 41, 2020, p. 415202.